JOURNAL OF GEOPHYSICAL RESEARCH: OCEANS, VOL. 118, 1–16, doi:10.1002/2013JC009165, 2013

A turbulent convection model with an observational context for a deep-sea hydrothermal plume in a time-variable cross flow

J. W. Lavelle,[1] Daniela Di Iorio,[2] and Peter Rona[3]

Received 29 May 2013; revised 9 September 2013; accepted 11 October 2013.

[1] A turbulent convection model for a hydrothermal fluid discharging into a tidally modulated, stratified cross flow is used to investigate time-variable conditions in plumes, such as the one rising from Dante, a sulfide mound at ~2175 m depth on the Endeavour segment of the Juan de Fuca Ridge. That plume is the consequence of the coalescence of 10 or more small, individual plumes from chimneys discharging hot, salt-diminished fluid into the near-bottom ocean. At Dante, the discharge encounters ambient horizontal currents with speeds oscillating from near zero to a maximum of ~7 cm s^{-1}, speeds which can bend a plume more than 45° from the vertical. Model results are compatible with field measurements of the plume footprint size and vertical velocity both 20 m above the source when earlier estimates for Dante's heat flux of ~50 MW drive the convection. The small-scale short period variability of velocities and properties distributions observed in the field is mimicked in model results. Plumes pool above a source during periods of weak cross flows but stream away from the source, with more diluted concentrations and lower rise heights, at other times. Plume distributions, at identical cross-flow speeds, differ whether the flow is accelerating or decelerating. Small changes in background hydrographic profiles create differences in rise heights comparable to those caused by large changes in source buoyancy flux. If put into an entrainment context, results suggest an entrainment coefficient (α_{EFF}) that varies from ~0.11 to ~0.025 with increasing height (2–76 m) above the source.

Citation: Lavelle, J. W., D. Di Iorio, and P. Rona (2013), A turbulent convection model with an observational context for a deep-sea hydrothermal plume in a time-variable cross flow, *J. Geophys. Res. Oceans*, *118*, doi:10.1002/2013JC009165.

1. Introduction

[2] Hot fluid injected into the ocean at the seafloor almost always enters an environment where tidal currents account for a substantial fraction of the energy in passing flow. The subsequent advection of rising hydrothermal plumes under those conditions is a story of fast flows that lead to substantial plume bending and effluent streaming away from the source and of slower flows that lead to more upright plumes and effluent pooling above the discharge site. Some of these effects on hydrothermal plumes were recognized long ago by *Rudnicki et al*. [1994] and were modeled in a simple way by *Wetzler et al*. [1998]. Detailed acoustic observations [e.g., *Jackson et al*., 2003; *Rona et al*., 2006] of hydrothermal plumes at the Main Endeavour Field (MEF) on the Endeavour segment of the Juan de Fuca Ridge, a deep sea crustal spreading center, and particularly measurements [*Xu and Di Iorio*, 2012] at the sulfide mound called Dante in the MEF have renewed our interest in how these turbulent plumes respond to time-variable flow and what model and measurements together can say about source heat flux and dependence on other external variables. In this paper, we report results from a 3-D, time-dependent convection model for sources discharging into time-variable cross flows and compare specific model results to measurements made of the rising turbulent plume above Dante and nearby Grotto.

[3] The literature on models of plumes in cross flows is extensive, though most studies have been restricted to *steady* cross flows. Reviews of that work include those of *List* [1982], *Hanna et al*. [1982], *Woods* [2010], and *Mahesh* [2013]. Plumes bent in steady cross flows have been modeled analytically by, e.g., *Fay* [1973], and numerically by, e.g., *Devenish et al*. [2010]. Models in the first category are often said to be integral models because an assumption of the similarity of variable distributions within the plume allows an integration of equations over all-but-one coordinate direction, resulting in a set of ordinary differential equations for the plume development. The seminal model in this category is that of *Morton et al*. [1956]. Closure of those equation sets still requires parameterizing entrainment. Full 3-D time-dependent numerical

[1]NOAA/Pacific Marine Environmental Laboratory, Seattle, Washington, USA.
[2]Department of Marine Sciences, University of Georgia, Athens, Georgia, USA.
[3]Institute of Marine and Coastal Sciences and Department of Earth and Planetary Sciences, Rutgers University, New Brunswick, New Jersey, USA.

Corresponding author: J. W. Lavelle, NOAA/Pacific Marine Environmental Laboratory, 7600 Sand Point Way NE, Seattle, WA 98115, USA. (j.william.lavelle@lavelle-associates.org)

2169-9275/13/10.1002/2013JC009165

models of rising plumes often include turbulence submodels, an aspect that obviates direct parameterization of entrainment, but turbulence models require their own closure assumptions. While more costly computationally than integral models, they provide more situational flexibility and permit modeling time variability and turbulence within the plume, making the plume representations more realistic.

[4] Three-dimensional time-dependent convection models of *hydrothermal plumes* in a cross flow are limited in number. *Lavelle* [1997] used a turbulent convection model to examine plume dependence on the Earth's rotation, turbulent mixing, and steady cross-flow speed. Using a cross-flow convection model, *Lavelle and Wetzler* [1999] examined the chemical concentrations in neutrally buoyant plumes following the mixing and ascent of diffuse-source and high-temperature hydrothermal fluids and ocean bottom water. More recently, *Tao et al*. [2013] have used a 3-D model with an irregular telescoping grid but without Earth's rotation to look at, among other things, the dependence of plume rise height on steady cross-flow velocity. Like that work, our model includes a turbulence submodel, but here importantly cross flow is time variable, effects caused by the Earth's rotation are allowed, and discharge temperature and salinity anomalies with respect to background both influence the plume's buoyancy. Examples of model plumes in nonrotating, nonstratified *oscillating cross flows*, are also few in number, e.g., *Xia and Lam* [2004] and *Kremer et al*. [2007], though neither study has a hydrothermal context. A brief review of observational and modeling work on deep-ocean plumes from high temperature hydrothermal discharges (i.e., smokers) has been provided by *Di Iorio et al*. [2012]. Plume measurements at Dante are described by *Xu and Di Iorio* [2012]. Plume measurements above Grotto, a neighboring sulfide mound at the MEF, are reported by *Jackson et al*. [2003], *Rona et al*. [2006], and *Bemis et al*. [2006].

[5] Dante is an irregularly shaped sulfide mound, ~15 m wide and ~30 m long, standing 25 m above the adjacent seafloor located at 129.0979°W and 47.9492°N (Lamont-Doherty's *Marine Geoscience Data System*, http://www.marine-geo.org/portals/ridge2000/vents.php). Vent locations for Endeavour segment sites were provided to the data portal by D. Kelley and D. Glickson of the University of Washington [*Merle*, 2006]. Dante's location is within the Main Endeavour Field (MEF) of the Endeavour segment of the Juan de Fuca Ridge [e.g., *Delaney et al*., 1992; *Kelley et al*., 2012]. The MEF is the second most southerly vent cluster of five prominent clusters in the ~10–15 km long hydrothermally active section of the Endeavour segment [e.g., *Veirs et al*., 2006; *Glickson et al*., 2007; *Kelley et al*., 2012]. All five major vent clusters sit within an axial valley that has walls 100–150 m high separated by ~1 km [e.g., *Delaney et al*., 1992]. *Stahr et al*. [2000] estimated that vents in the MEF together release heat at the rate of 650 MW; *Delaney et al*. [1997] and *Veirs* [2003] summarize earlier heat flux estimates.

[6] Dante is just one of many venting complexes (e.g., sulfide mounds) at MEF discharging high temperature hydrothermal fluids [*Delaney et al*., 1992; *Cruse and Seewald*, 2010]. Dante alone hosts 10 or more high-temperature small smokers distributed over its top surface [*Delaney et al*., 1992]. Visual observations by the remotely operated vehicle Jason2 and the manned submersible Alvin together with acoustic imaging at Dante suggest the plumes from individual smoker sources coalescence within a few vertical meters of the top of the mound [*Xu and Di Iorio*, 2012]. *Jackson et al*. [2003] report from video observations at the neighboring sulfide mound Grotto that five individual plumes from vents within an area of 3 m × 3 m had coalesced at a height 4–5 m above source depth. *Rona et al*. [1991] also observed two plumes with sources separated laterally by only ~3.5 m merging in a vertical distance of ~8 m above the top-most chimney orifice. Plume coalescence from multiple sources in other settings has been measured in the laboratory and/or modeled by, e.g., *Kaye and Linden* [2004] and *Yamamoto et al*. [2011]. It is the coalesced plume from multiple too-small-to-resolve vent chimneys that we model in this paper.

2. Model Design

[7] The model is a 3-D time-dependent turbulent convection model. Convection is induced by the release of hot, salt-diminished fluid from a localized source on the seafloor into a moving, stratified, rotating (*f*-plane) overlying ocean. The model is a version of the one described by *Lavelle* [1997], enhanced to allow time-dependent cross flow, simpler open boundary conditions, and separate horizontal and vertical mixing parameterizations. The model geometry is that of a parallelpiped into which fluid, heat, and salt are injected at the lower surface; the model design currently disallows variations of bathymetry within the computational domain. Together with the UNESCO equation of state for seawater [*Fofonoff and Millard*, 1983], the following equations summarize this model's physics:

$$\frac{\partial}{\partial t}\vec{u}+\vec{u}\cdot\nabla\vec{u}=-\nabla p/\rho_0-2\vec{\Omega}\times\vec{u}+\nabla\cdot(A\nabla\vec{u})-\hat{k}g\rho/\rho_0 \\ -\vec{\alpha}\cdot(\vec{u}-\vec{u}_{bkg})+\vec{F}_B \tag{1}$$

$$\nabla\cdot\vec{u}=0 \tag{2}$$

$$\frac{\partial}{\partial t}(\theta,S,C)+\vec{u}\cdot\nabla(\theta,S,C)=\nabla\cdot\Big(K\nabla(\theta,S,C)\Big) \\ +Q_{\theta,S,C}-\alpha_S\Big((\theta-\theta_{BKG},S-S_{BKG},C-C_{BKG})\Big) \tag{3}$$

$$A=(A_H,A_H,A_V) \tag{4}$$

$$A_H=(C_{sh}l_{sh})^2(2\tilde{S}_h{}^2)^{\frac{1}{2}}+A_{HMIN} \tag{5}$$

$$A_V=(C_{sv}l_{sv})^2(2\tilde{S}_v{}^2)^{\frac{1}{2}}(1-Ri/\mathrm{Pr})^{\frac{1}{2}}+A_{VMIN} \tag{6}$$

$$\tilde{S}_h{}^2=\left[\left(\frac{\partial u}{\partial x}\right)^2+\left(\frac{\partial v}{\partial y}\right)^2+\frac{1}{2}\left(\frac{\partial u}{\partial y}+\frac{\partial v}{\partial x}\right)^2+\frac{1}{2}\left(\frac{\partial w}{\partial x}\right)^2+\frac{1}{2}\left(\frac{\partial w}{\partial y}\right)^2\right] \tag{7}$$

$$\tilde{S}_v{}^2=\left[\frac{1}{2}\left(\frac{\partial u}{\partial z}\right)^2+\frac{1}{2}\left(\frac{\partial v}{\partial z}\right)^2+\left(\frac{\partial w}{\partial z}\right)^2\right] \tag{8}$$

$$K=(A_H,\ A_H,\ A_V)\ /\mathrm{Pr} \tag{9}$$

[8] Here t is time, $\vec{u}$ represents time-varying component velocities (u, v, w) in the along-axis, cross axis, and vertical directions, respectively, with w positive upward. Retention of the substantial derivative terms in the w momentum equation makes the model nonhydrostatic. The variable p is pressure, ρ is density, ρ_0 (1025 kg m^{-3}) is a fixed reference density, g (9.81 m s^{-2}) is the acceleration of gravity, $2\vec{\Omega}$ (π sin (47. 95°)/12 h = 1.08 $\times$ 10^{-4} s^{-1}) is the local vertical component of the Earth's rotation vector, $\hat{k}$ is a unit vector in the vertical direction, and F_B is a body force. The manner of choosing F_B is explained below.

[9] Potential temperature (θ), salinity (S), and the dynamically inert tracer C fields depend on $\vec{u}$, on diffusivity coefficients (K_H, K_V) in the horizontal and vertical directions, and on source flux rates, e.g., Q_C. The functions θ_{BKG}, S_{BKG}, and C_{BKG}, dependent only on z, are background profiles. The heat equation takes the form of a potential temperature equation after multiplicative constants ρ_0 and C_P are canceled in each term of the heat equation. C_P is the specific heat of water (4200 J kg^{-1}°C^{-1}). In actuality, a much higher C_P ($\sim$6200 J kg^{-1}°C^{-1}) is more appropriate for high temperature ($\sim$>350°C) hydrothermal vent discharge, but that increase is offset in the product ρ_0 C_P by the fact that the density of the same high temperature fluid is the order of 600 kg m^3 [*Burnham et al*., 1969; *Bischoff and Rosenbauer*, 1985]. Moreover, high effluent temperatures are quickly reduced by mixing with cold ambient ocean water to temperatures <$\sim$40°C. Below that value to freezing and for $0 < S < 42$ psu the UNESCO equation of state [*Fofonoff and Millard*, 1983] is appropriate.

[10] Viscous mixing coefficients in the horizontal (A_H) and vertical (A_V) directions depend on velocity shears via the functions $\tilde{S}_H^2$ and $\tilde{S}_V^2$ and on grid length scales (e.g., l_{SH} and l_{SV}) [*Smagorinsky*, 1993]. C_{SH} and C_{SV}, the Smagorinsky coefficients, were given values of 0.14 and 0.04, which are within the range of values commonly used [*Smagorinsky*, 1993]. The lengths l_{SH} and l_{SV} took values of (dx dy)$^{1/2}$ and dz, respectively, where dx, dy, and dz represent computational cell lengths. Small constant terms ($A_{HMIN} = 5 \times 10^{-4}$ m^2 s^{-1} and $A_{VMIN} = 5 \times 10^{-5}$ m^2 s^{-1}) were added to the variable parts of A_H and A_V to ensure a modicum of mixing in regions of little velocity shear. The magnitude of A_{VMIN} is comparable to that estimated for the quiet, interior ocean [*Ledwell et al*., 1993; *Kunze and Sanford*, 1996]. Where turbulence isotropy is the norm, the shear square terms are not often separated into functions $\tilde{S}_H^2$ and $\tilde{S}_V^2$, but ocean stratification breaks the isotropy. A_H and A_V are related to the corresponding eddy diffusivities (K_H and K_V) via a fixed Prandtl number Pr (= 3.0). The ratio of Ri (i.e., the shear Richardson number) to Pr was also held at a fixed value of 0.167. These values are similar to those of *Venayagamoorthy and Stretch* [2010], for example, when $Ri \sim 0.5$.

[11] The terms involving functions $\vec{\alpha}$ and α_S are used to suppress reflections at open boundaries of all outwardly propagating waves generated in the domain interior and allow, in effect, the outward passage of plume material through the same boundaries [e.g., *Lavelle and Thacker*, 2008]. These "pretty good sponge" functions are nonzero only over thin regions at the edges of the computational domain. Their magnitudes grow quadratically over typically a 10 cell distance from zero to values at the domain walls that were consistent with the Courant condition for integrating stiff equations [*Lavelle and Thacker*, 2008]. The u and v velocities are sponged only in the x direction and in the y direction, respectively, while variables w, θ, S, and C are sponged on all four lateral (open) boundaries and on the closed boundary of the domain lid. The lid sponge suppresses reflections of upwardly propagating waves, whatever their origin.

2.1. Numerical Considerations and Boundary Conditions

[12] Equations (1–9) were solved in flux-conservation form on a computational C-grid having dimensions of 192 $\times$ 128 $\times$ 162 (or 192 or 216) and a uniform cell size (dx, dy, dz) of (1.0, 1.5, and 2.0 m). The momentum equations were integrated implicitly using the method of *Harlow and Welch* [1965] with leapfrog time steps. The Assel coefficient [*Assel*, 1972] was 0.0075 while the size of the time step varied over experiments but was always at or near 1 s; the number of time steps typically was 129,600. The transport equations were forward-time and upstream-space differenced, with numerical diffusion suppressed using the MPDATA scheme of *Smolarkiewicz and Margolin* [1998] having two correction cycles. *Lavelle* [1997] provides additional details.

[13] The source region of hydrothermal heat and salt release was limited to a small seafloor area around the grid center ($x = 0$, $y = 0$), which itself was shifted in the model domain to a point 1/3 along the length of the domain x axis, the x axis being the primary advection direction. Buoyancy was injected at the domain's lower edge, making the sulfide mound's top surface the origin for the z axis. The source area varied over the set of experiments from 6 m $\times$ 6 m to 4 m $\times$ 4.5 m to 3 m $\times$ 3 m (Table 1).

[14] Over the rectangular seafloor source region (Table 1), the discharge was made to be jet-like with a uniform upward velocity (w) of 0.1 m s^{-1}. To conserve mass, an equivalent flux was directed into the seafloor over all the remaining cells of the unsponged region. Replacing egressing hydrothermal fluid from the Earth's crust with ocean near-bottom water must actually occur in nature [*Johnson et al*., 2010] though the specifics of the actual fluid recharge still are poorly known. Recharge flow speeds were $\sim$1 $\times$ 10^{-4} m s^{-1}.

[15] The model domain was open on all four lateral sides and closed on the top and on the bottom with the exception for vertical flow in and out of the bottom as described. The lateral boundary conditions for all variables (u, v, w, θ, S, p) were simple zero derivative conditions (e.g., $\partial v/\partial y = 0$, $\partial\theta/\partial x = 0$) in both x and y directions. This is possible because the sponge terms in equations (1) and (3) draw the velocities and hydrographic/tracer variables back to background values in peripheral regions where the αs are nonzero. Vertical gradients of all but the vertical velocity were given zero value at both the domains top and bottom; bottom stress was zero because the computational domain's bottom edge ($z = 0$) corresponds to the top of the sulfide mound (2175 m), which is the seafloor only over a small fraction of the total area of the domain. At the domain lid, w was set to zero; the inflow-outflow at the domain floor has already been described.

[16] Fluid motion is caused by a body force, F_B, derived from background currents u_{BKG} and v_{BKG} by asserting that

Table 1. Parameter Variations Over Each of the Six Numerical Experiments Reported

	Source Area	Heat Flux	Domain Upper Edge	Domain Stratification
Exp. 16	6 m × 6 m	50 MW	1851 m	Linear
Exp. 17	4 m × 4.5 m	50 MW	1791 m	Linear
Exp. 19	4 m × 4.5 m	50 MW	1791 m	Nonlinear
Exp. 20	4 m × 4.5 m	20 MW	1791 m	Nonlinear
Exp. 21	4 m × 4.5 m	80 MW	1743 m	Nonlinear
Exp. 22	3 m × 3 m	50 MW	1791 m	Linear

the principal momentum balance at the domain periphery under nonconvecting barotropic conditions is represented in the following equation:

$$\frac{\partial}{\partial t}\vec{u}_{BKG} = -2\vec{\Omega}\times\vec{u}_{BKG} + \vec{F}_B \tag{10}$$

[17] This is the approach used in *Lavelle* [1997]. F_B might be viewed as a spatially uniform but temporally varying sea surface gradient. F_B was ramped so that the fluid would be spun-up from rest over the initial two simulation hours. Model results were recorded 24 times each M_2 period over the first 36 h. In one experiment, data were recorded every second over three 5 min intervals for use in entrainment analysis.

2.2. Background Currents, Hydrography, and Source Discharge Rates

[18] *Thomson et al*. [2003] measured currents deep within and above the Endeavour segment axial valley at a site approximately 1 km north of the MEF. Their deepest current data showed that the M_2 tidal and mean currents were the most energetic components of the flow. Smaller spectral peaks occur at diurnal periods and at 4 days. The M_2 tidal ellipse has a major axis of 3.6 cm s^{-1} oriented nearly along the axial valley and a minor axis of 0.25 cm s^{-1}. Mean flow was also primarily in the direction of the axial valley at 3.15 cm s^{-1}. Based on spectral energy content and with a need for cyclicity in model results for a time integration of manageable length, background flows in x and y directions past Dante were idealized to be:

$$u_{BKG} = u_0 + u_1 \sin(2\pi t/T) \tag{11}$$

$$v_{BKG} = v_0 + v_1 \cos(2\pi t/T) \tag{12}$$

where $T = 12.42$ h and coefficients $(u_0, v_0) = (3.15, 0.0)$ cm s^{-1} and $(u_1, v_1) = (3.6, 0.25)$ cm s^{-1}. The x axis of the model is oriented in the common direction of the mean flow and the major axis of the M_2 tidal ellipse.

[19] The current shear that *Thomson et al*. [2003] observed and *Thomson et al*. [2005] and *Berdeal et al*. [2006] both modeled in and above the axial valley is not addressable with the present convection model because the model does not encompass variable topography. On the other hand, outside a thin boundary layer, the velocity shear can be expected to be small for the few tens of meters above the source, where many of the acoustic measurements of hydrothermal plumes have been made. Consequently, it is nearest the model seafloor where the model results could be expected to be most like observations, though above that height the model can still inform us about plume features in a more general way.

[20] Background hydrography was given two forms. In three experiments (Table 1), the hydrography was based on measurements made outside the axial valley. Those data [*Xu and Di Iorio*, 2012] showed near linearity of potential temperature and salinity with depth over the lower part of the water column. Based on those measurements, the first set of background profiles (linear hydro) were:

$$\theta_{BKG} = 1.673 - 6.666\times10^{-4}(z - z_S) \tag{13}$$

$$S_{BKG} = 34.612 + 1.135\times10^{-4}(z - z_S) \tag{14}$$

$$C_{BKG} = 0.0 \tag{15}$$

where z ranged from z_S (= 2175 m) to as shallow as 1743 m.

[21] In other experiments (Table 1), the background hydrography was based on data from a tow-yo CTD transect made within the MEF axial valley and passing over Dante on 21 September 2007. The transect started at 47.9515°N, 129.0963°W and finished at 47.9464°N, 129.1002°W. θ and S from three down casts that did not evidence any clear effects of nearby hydrothermal discharge were averaged to create the second set of background profiles (nonlinear hydro, Figure 1). The use of these profiles acknowledges the near certainty that the hydrography in the vicinity of active sulfide mounts is altered by prior vent discharges. Juxtaposing plume results from the two sets of profiles (Figure 1) allows examination of the sensitivity of model results to minor changes in hydrography.

[22] The source fluid was given a salinity of 29.3 psu [*Butterfield et al*., 1994]. The fluid thus had added buoyancy as the result of it being ~5.3 psu fresher than the surrounding ocean (Figure 1). The total heat flux at the source was allowed to range from 20 to 80 MW (Table 1). *Ginster and Mottl* [1994] estimated the heat discharge of Dante to be 87.3 MW based on direct measurements at several black smokers and on the total number of smokers observed. *Bemis et al*. [1993] estimated the heat flux to be in the range of 29.3–88.4 MW at Dante based on similar type measurements and extrapolations.

3. Field Measurements of the Buoyant Plume Compared to Model Results

[23] Several type of measurements of the plume over Dante are available for qualitative comparisons to model results: average vertical velocities in the plume at 20 m above the venting level, the cross-sectional diameter of the plume at 20 m, and several CTD profiles from the axial valley near Dante that evidence hydrothermal discharge. Acoustic backscatter observations of Grotto [*Jackson et al*., 2003] also corroborate the occurrence of fine-scale spatial and temporal variability of the plume that is conspicuous in model results.

[24] *Xu and Di Iorio* [2012] measured spatially averaged vertical velocity in the plume at a height 20 m above the

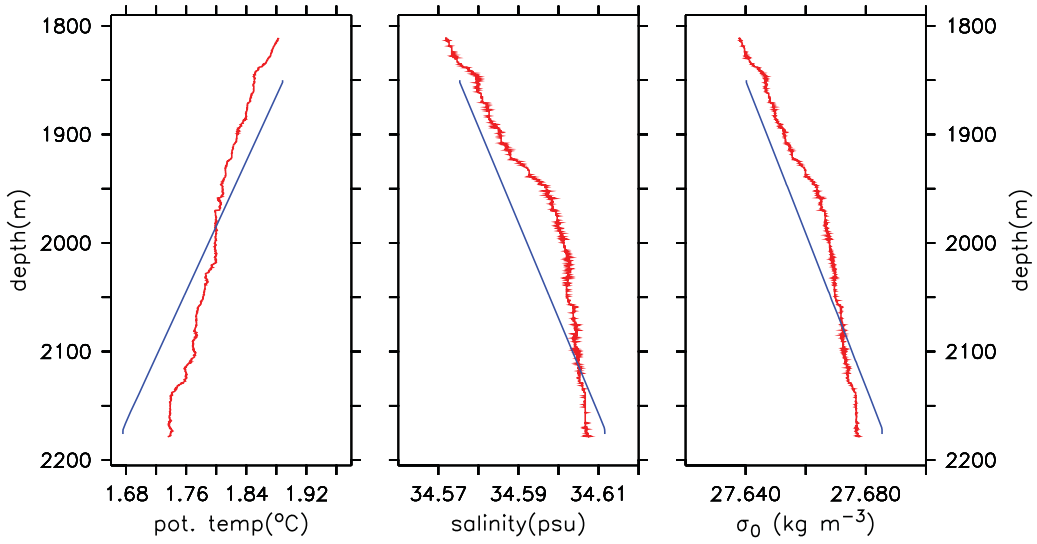

Figure 1. Potential temperature, salinity, and σ_0 from measurements outside of the Endeavour axial valley after fitting a linear regression line ("linear hydro," blue) and an estimate of "background" profiles within the axial valley in the vicinity of the Main Endeavour Field based on a CTD tow-yo ("nonlinear hydro," red). The buoyancy frequency of the linear profiles is 1.11×10^{-3} s^{-1}.

summit of Dante by acoustic scintillation. Their results suggest plume $\langle w \rangle = \sim 0.15$ cm s^{-1} at times of near zero cross flow. A model snapshot of vertical velocity in the *x-z* plane over Dante (Figure 2a) shows a plume rising some 200 m above its source. To calculate model plume spatial averages, a plume edge criterion must be set. We arbitrarily use two possible criteria for the plume edge: where $w = 0.02$ m s^{-1} or where $C_{REL} = C/C_{MAX} = 0.1$. C_{MAX} is the maximum value of the dynamically inert tracer C in the volume or on the plane of interest. The second criterion is analogous to choosing an edge value >2 standard deviations below the maximum if concentrations were distributed in Gaussian fashion. The model $\langle w \rangle$ in Figure 2a on the plane 20 m above Dante is 0.07 m s^{-1} using the velocity criterion and 0.089 ms^{-1} using the C_{REL} criterion. If the edge criteria are amended to be $w = 0.05$ m s^{-1} or $C_{REL} = 0.3$, the corresponding $\langle w \rangle$ are 0.103 and 0.122 m s^{-1}, incrementally more like the measurements.

[25] The same small spatial scale (~1 m) variability (Figure 2a) is made clearer by stacking 15 cm s^{-1} velocity

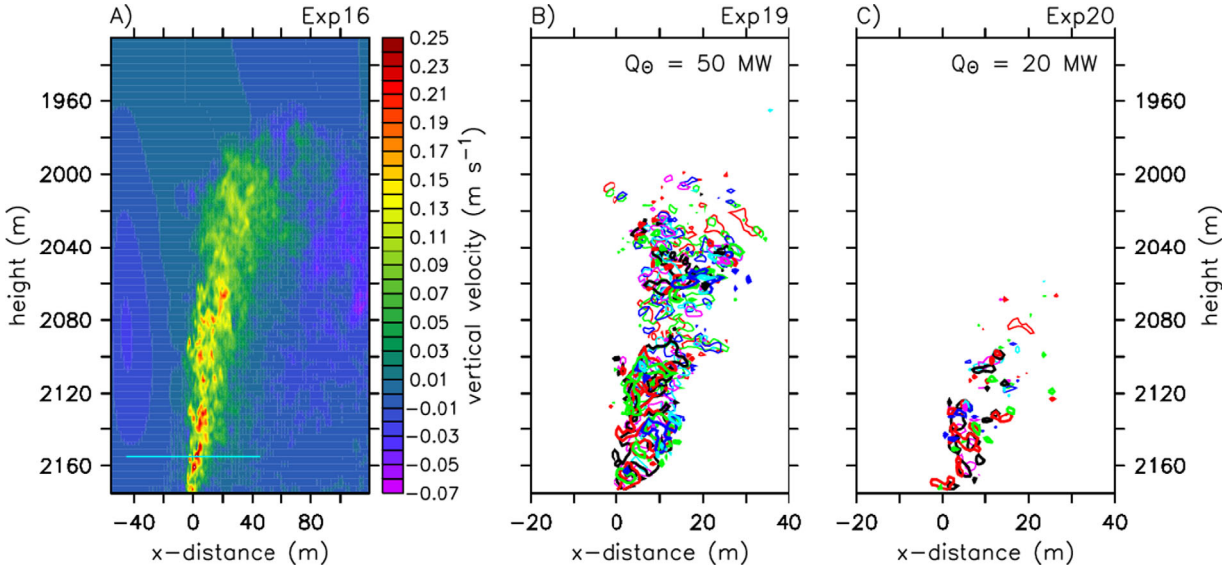

Figure 2. (a) Model vertical velocities (w) on the plane at $y = 0$ at a time of near zero decelerating cross flow from Exp. 16 (Table 1). The cyan blue line represents the location of the path of acoustic scintillation measurements from which vertical velocities and temperature variances at 2155 m depth (~20 m above Dante vents) were estimated [*Xu and Di Iorio*, 2011, 2012]. In the other two plots, contours of the 15 cm s^{-1} isovel on 14 equidistant *x-z* planes (-9.5 m $< y <$ 9.5 m) are represented with varying colors for (b) Exp. 19 (50 MW) and (c) Exp. 20 (20 MW).

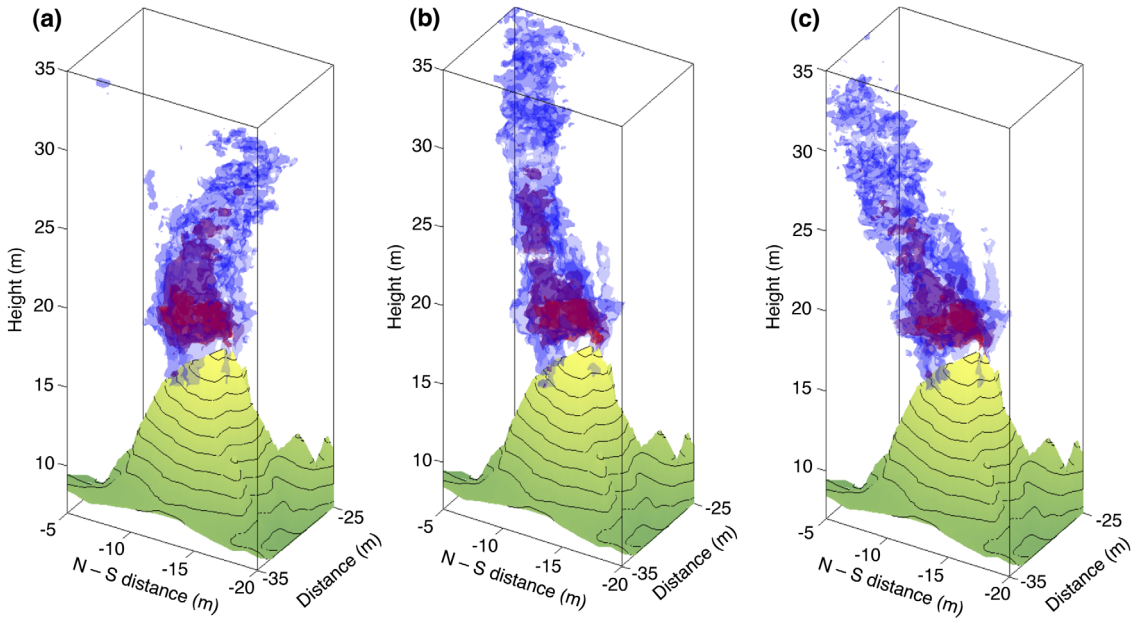

Figure 3. The hydrothermal plume above the north tower of the sulfide mound Grotto in the Main Endeavour Field as imaged on 15 May 2013 at (a) 3, (b) 12, and (c) 18 h UTC. Measurements were made using the Cabled Observatory Vent Imssaging Sonar (COVIS) [*Rona and Light*, 2011]. Acoustic backscatter intensity decreases, i.e., plume dilution increases, by a factor of 10 over each step through the sequence of red, purple, and blue isosurfaces. *In (a) t*he plume bends slightly to the south, in Figure 3b the plume rises approximately vertically, and in Figure 3c the plume bends more strongly to the north. Horizontal position units are relative to the location of COVIS.

isopleths (Figure 2b). The figure is a composite of contours on 14 separate *x*-*z* planes spanning the *y* interval -9.5 m $< y <$ 9.5 m at 1.5 m increments. The bulk of the contour lines fall below a depth of 2050 m, some 125 m above the source. Similar variability of velocity isosurfaces has been seen in acoustic backscatter measurements of the primary plume at nearby Grotto [*Jackson et al*., 2003; *Rona et al*., 2006], at Monolith vent on the Cleft segment of the same spreading ridge [*Bemis et al*., 2002], and at EPR 21°N [*Rona et al*., 1991]. A notable difference in model results (Figure 2b) and the observations just cited is that the height reached by the 15 cm s^{-1} model isovels is considerable higher than in observations. Those differences must be caused by site differences, e.g., hydrography or heat output. Hydrography cannot be a factor in the case of Grotto because of its close proximity to Dante (∼40 m center to center), but heat output may be. When Figure 2b is redone using Exp. 20 model data (20 MW versus 50 MW heat output), the number of 15 cm s^{-1} contours is greatly reduced and the vast majority of them occur within 45 m vertically of the source (Figure 2c). This suggests that composite source heat (and buoyancy) flux strongly influences vertical advection speed. Rise height, on the other hand, is known to have a weak dependence on buoyancy flux. More emphasis on measuring the vertical velocity in plumes tens of meters above a venting complex is thus suggested.

[26] Measurements of the plume rising from the north tower of Grotto, a sulfide mound within 40 m of Dante, show plumes (Figure 3) bending with passing currents and having small spatial-scale intensity variations that can be attributed to turbulence in the rising plume. The underlying data were acquired with COVIS (Cabled Observatory Vent Imaging Sonar) [*Rona and Light*, 2011], a device that measures acoustic backscatter from turbulent temperature variations and plume particles; engineering concepts and sampling methodology are described by *Xu et al*. [2013]. In this case, every 3 h over a 40 min time period, COVIS's wide but thin (1°) acoustic beam swept up and down 37° vertically in 1° stepped increments. Scattering intensity values were subsequently assigned to volume elements (0.5 m × 0.5 m × 0.5 m) of a parallelpiped (Figure 3). The red, purple, and blue isosurfaces in each plot of Figure 3 are based on an average of intensity values that fell within each small volume element during each 40 min set of stepped vertical sweeps. The resulting relative acoustic scattering intensities, at three well-separated times, show plumes bending differently in response to time-variable ambient (unmeasured) currents. In Figure 3a, the plume tilts slightly to the south, while in Figure 3b, presumably near slack water, the plume is nearly vertical. The larger, northward tilt of the plume in Figure 3c is more representative of the tidally modulated, mean advective flow to the north encompassed in this paper's model.

[27] A close look at the region near the top of mound (Figure 3) shows that the plume aloft results from the coalescence, after a few meters rise, of plumes from individual sources near the top of Grotto. These data further imply that the southernmost source on the north tower is the most turbulent or most particle-laden, and thus probably contributes a larger flux of heat than the others. The small spatial-scale variability visible in the scattering signal in each plot of Figure 3 is a recurrent feature of the model variable distributions.

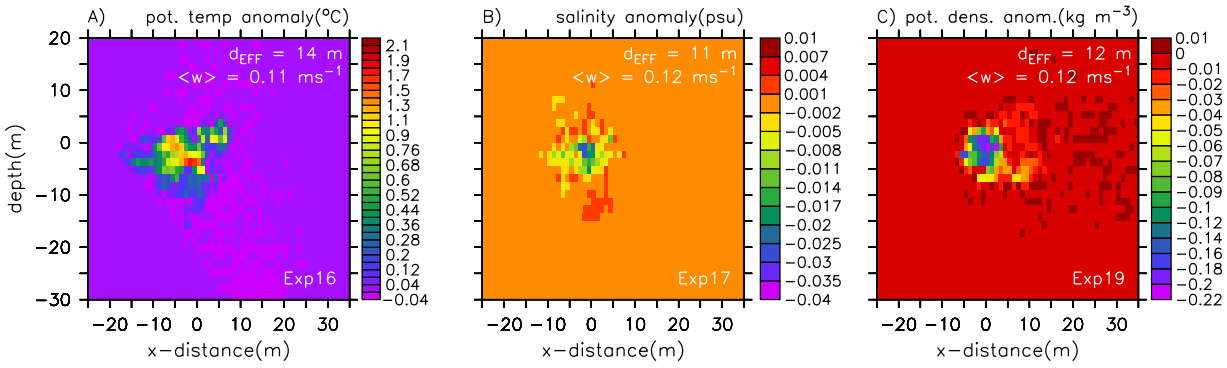

Figure 4. Footprints of plumes as temperature, salinity, and potential density anomalies for, in sequence, Exps. 16, 17, and 19. Each is an instance of a distribution at $z = 2155$ m at a time of near zero cross flow. All three experiments represent the same source buoyancy flux. The label d_{EFF} is the diameter of a circle having the same area as cells for which $C/C_{MAX} > 0.1$. $\langle w \rangle$ is the vertical velocity at the same height, averaged over the same cells.

[28] Model plume footprints indicate effective footprint diameters (d_{EFF}) ranging from 11 to 14 m at 2155 m (Figure 4). The depth of 2155 m, cited often in what follows, represents a level approximately 20 m above the vent orifices at Dante. Effective footprint diameters are those of circles the area of which are equal to the sum of the areas of all model grid cells at any one level that exceed the C_{REL} threshold. Over three experiments (Figure 4), Exp. 16 has the largest effective diameter (14 m) at depth 2155 m, but it also has the largest area (36 m^2) at the source. Exp. 17 has a smaller source area by a half (Table 1) and a smaller d_{EFF} by 21% vis a vis Exp. 16. The larger d_{EFF} in Exp. 19 versus Exp. 17 is a result of a change only in the background stratification profile.

[29] These footprints are irregular in shape, and more oval than circular, even though these snapshots represent the plume at a time of minimum horizontal advection speed ($u_{BKG} = 8.2 \times 10^{-4}$ m s^{-1}). The irregularity in cross sections and concentrations is supported by the observations of *Bemis et al*. [2002], *Rona et al*. [2002], and *Jackson et al*. [2003] at other venting sites. A downward looking acoustic backscatter multibeam image of the plume taken by the ROV Jason2 hovering 30 m above Dante [*Xu and Di Iorio*, 2012] suggests a value of ~14 m for the diameter of the plume at the height of these footprint results. The ROV measurements, however, do not address the circularity or noncircularity of the plume at this level, so the 14 m diameter value can only provide a semiquantitative target for the model plume diameter at that height.

[30] The CTD tow-yo transect (section 2.3) provided two θ and S profiles (Figure 5, red and magenta) indicative of proximity to active hydrothermal discharge sites. In those profiles (Figure 5), the maximum thermal anomaly is as much as 0.2°C, while the salinity anomaly is noise-like. At one of the two locations, the anomaly begins very near the seafloor and extends to ~2125 m, while at the other, the anomaly begins higher up at 2160 m and extends above 2100 m. The anomalous fluid is buoyant (Figure 5c).

[31] Model profiles (Figure 6) demonstrate some of the same features as the observations. Profiles in red (Figure 6) were taken 10 m downstream of the discharge region when the plume is bending, though not maximally, in the cross flow. The heat anomaly disappears before reaching a height of 2100 m because of that bending. The second (magenta) profile is taken an additional 10 m downstream where the plume has separated more from the seafloor and the top edge is located higher in the water column. The salinity anomalies (Figure 6b) are both small as they were in Figure 5b. The likenesses between modeled and observed profiles are particularly encouraging, but the comparison is only qualitative because the model is highly idealized and field profile locations with respect to actual sources are not well determined.

4. Expanded Model Results

[32] Six experiments (Table 1) were conducted to examine systematic differences in plumes as cross-flow cycled, and when source heat flux, hydrographic profiles, and source areas were varied. The number of experiments was limited by the calculation time (4–6 days, 6–12 processors) required for each and by the size (typically 61G) of each resulting data set.

4.1. Dependence on Cross-Flow Speed

[33] The effect of mean plus tidal cross flow on hydrothermal plumes is exemplified in the vertical velocity plots of Figure 7. The sequence (Figures 7a–7d) is (a) when cross-flow speed is 34% of maximum and accelerating; (b) at maximum speed; (c) again when cross-flow speed is 34% of maximum but decelerating; and (d) near zero u velocity. The differences in plumes in Figures 7a and 7c are notable because both were sampled at times of identical cross-current speed (0.023 m s^{-1}). The causal difference is that Figure 7a represents an accelerating flow and Figure 7c a decelerating flow. In Figure 7a, the plume is starting to lose height by bending, while in Figure 7c, the plume is recovering height after a time of maximum cross flow (Figure 7b). The acceleration stage has other consequences too, as will be elucidated later. Maximum cross flow bends the plume 52° from the vertical (Figure 7b). Turbulence causes fine-scale variations in w of the kind observed by *Jackson et al*. [2003].

[34] As the plume bends in the cross flow, its footprint on horizontal planes ordinarily grow larger. Contours of

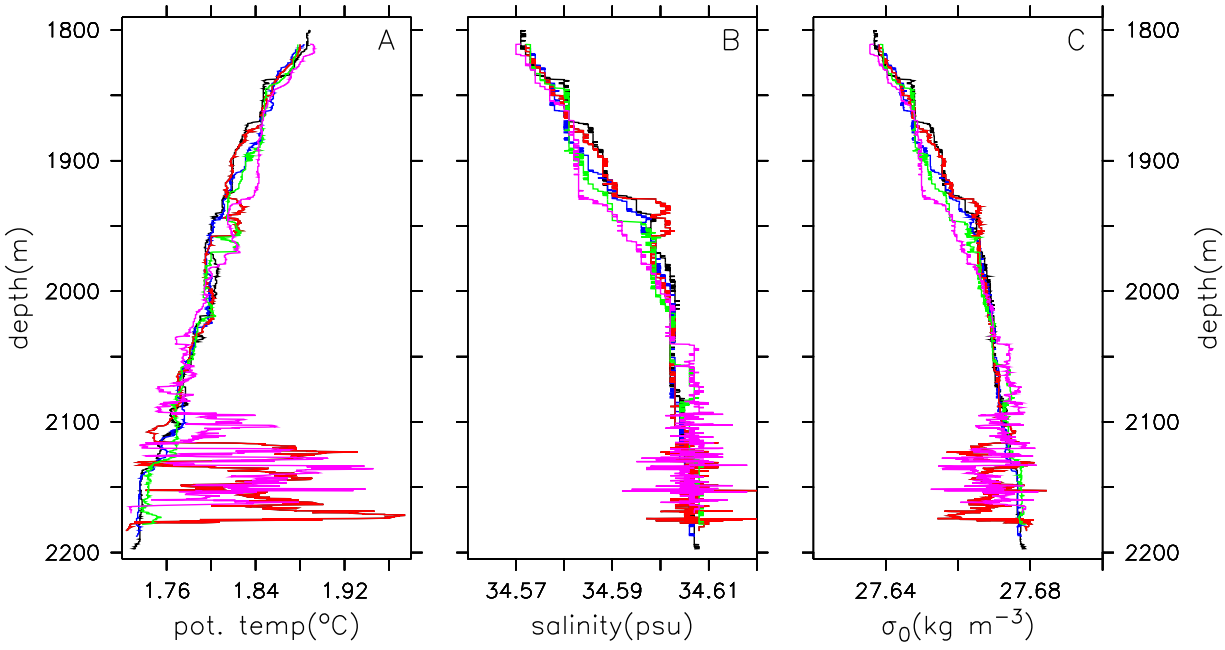

Figure 5. Hydrography from five down casts taken on a single ~600 m long tow-yo transect down the axis of the MEF axial valley, starting NNE of and then over Dante and on toward the Bastille-Puffer hydrothermal edifice complex (e.g., vide map in Cruse and Seewald [2010]). Profiles in purple and red show the effects of hydrothermal discharge, including negative buoyancy below 2100 m depth. The three other θ and S profiles were averaged to provide the nonlinear hydrography depicted in Figure 1.

$w = 0.1$ m s^{-1} on the plane $z = 2155$ m over a full tidal cycle (Figure 8) show the "center of mass" of the w plume moving downstream and then back over the source in this oscillatory flow. At largest cross flow, the footprint extends as much as 30 m from the source center. Multiple closed contours of any one color document plume fractionation consistent with the turbulent nature of the rising fluid. In the Flow-Mow experiment, *Stahr et al*. [2000] surveyed

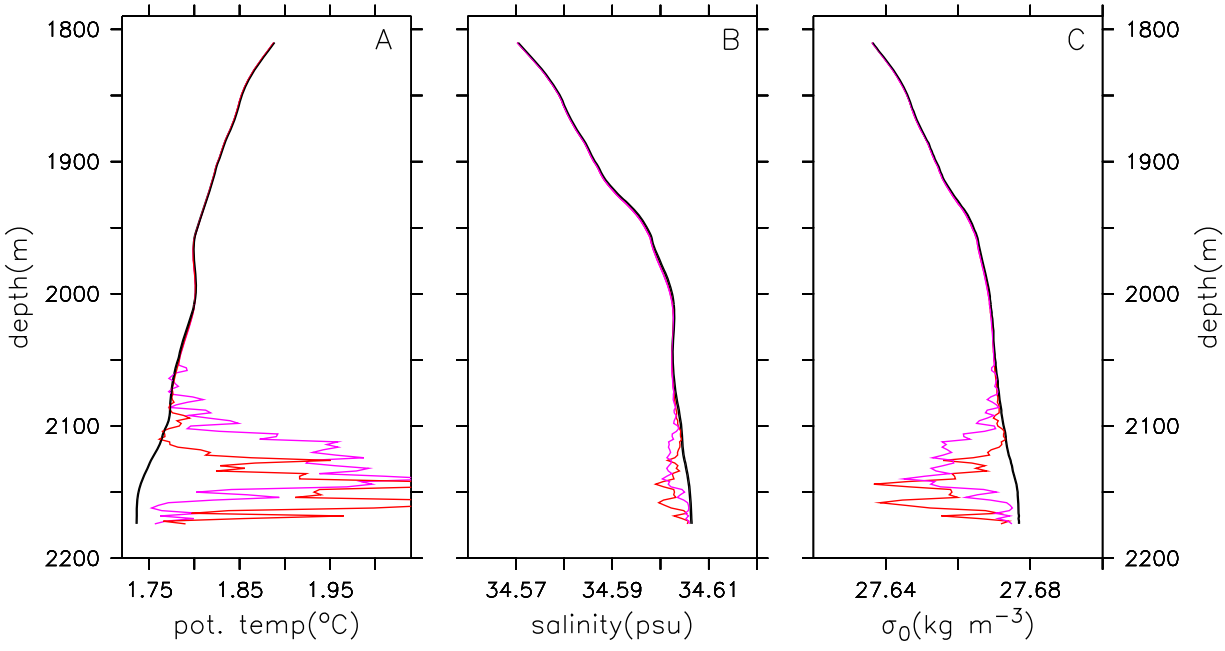

Figure 6. Model hydrographic profiles taken in the near vicinity of the model source after averaging over the interval -9.5 m $< y < +9.5$ m to suppress some of the small-scale variability. Downstream sampling locations were selected so that model profiles would have the character of those measured in Figure 5.

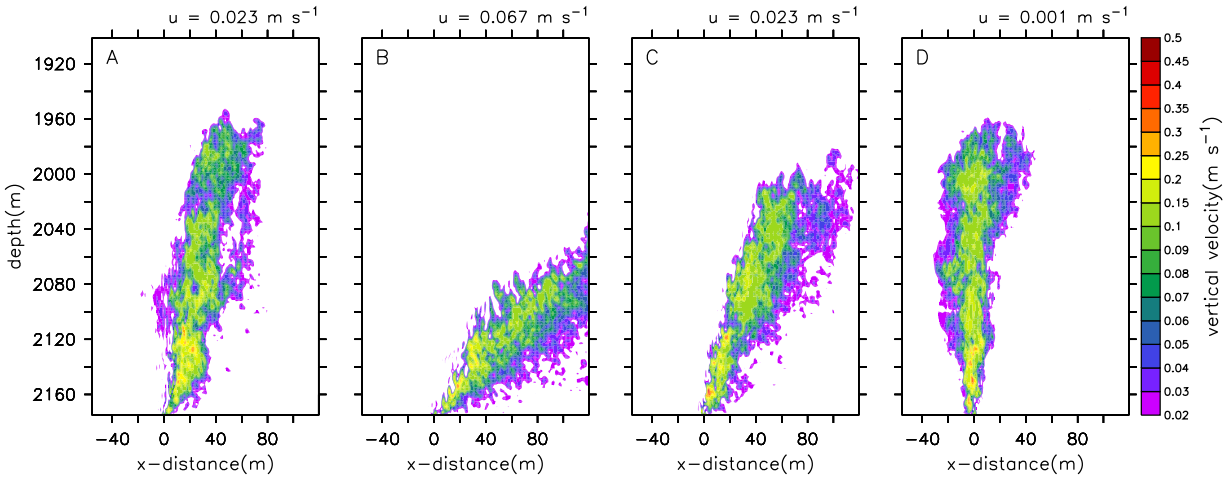

Figure 7. Vertical velocity in the plume on the *x*-*z* plane at $y = 0$ at four times in the cross-flow cycle: (a) cross flow at speed 2.3 cm s^{-1} and accelerating in the x direction (north); (b) cross flow at maximum northward velocity; (c) cross flow decelerating, but at identical speed as in Figure 7a; (d) cross flow accelerating to the north from its minimum. Exp. 17.

temperature over a sinuous pattern of closely spaced survey lines all on a horizontal plane ~90 m above the MEF axial valley floor using the Autonomous Benthic Explorer (ABE) [e.g., *German et al*., 2008]. Temporal variations in the temperature field similar to those of Figure 8 must have occurred during the course of the *Stahr et al*. [2000] measurements, but the multiple vent complexes at the MEF, the time-offset survey lines, and the overlapping footprints from separate plumes would further compound an already difficult interpretation of such measurements.

[35] The vertical velocity at $z = 2155$ m averaged over computational cells where $w > 0.02$ m s^{-1} is inversely correlated (Figure 9a) with the *x* axis flow velocity, i.e., when cross-flow *u* flow is strongest, the average value of *w* tends to be smallest, and vice versa. An inverse correlation between $\langle w \rangle$ and *u*, implicit in Figure 9a, has been observed in acoustic scintillation measurements at Dante [*Di Iorio et al*., 2012], though in the field measurements $\langle w \rangle$ depends on *u* more strongly.

[36] The plume footprint area must grow larger at small $\langle w \rangle$ and smaller at larger $\langle w \rangle$ if near constant vertical heat flux across any horizontal plane is to be maintained. That is exactly the case: using $C_{REL} > 0.1$ as the criterion for the plume edge, plume area on the plane $z = 2155$ m is negatively correlated with plume $\langle w \rangle$ (Figure 9b). In Figure 9b, points in the top left are those associated with large cross flows, while those in the bottom right correspond to conditions of small cross flow. Heat conservation as a time average actually requires tracking horizontal as well as vertical heat fluxes, but at small enough distances above the source (e.g., $z = 2155$ m), the bulk of the heat flux is vertical.

[37] The image of a plume depends on the variable that is used to generate it. Consider Figures 7 and 10 juxtaposed. The first set of plots is the plume expressed via *w*, while the second set is the plume expressed via the dynamically inert tracer *C*, though integrated over the y direction (-84 m $< y < 84$ m). In both Figures 7 and 10, the first plot represents a time of cross-flow acceleration after a period of near slack flow. During slack flow, *C* accumulates in the neutrally buoyant region over the source, after which, as in Figure 10a, the accumulation has begun to be advected downstream (to the right). The accumulated mass in Figure 10a has advected out of the model region by the time (7.25 h later) cross flow is at its maximum (Figure 10b). As flows begin to decelerate (Figure 10c), the height of the plume top increases as do concentrations within most of the plume volume. As advection again slows toward zero, the plume continues to grow in size and concentration around the level of neutral buoyancy (Figure 10d), but total *C* mass is less in Figure 10d than in Figure 10a because the period of slack water is just beginning. Said differently, the tracer *C* pools above the source around the time of slack water and streams away from the source with reduced concentrations when cross flow grows large. Pooling and streaming of plumes was highlighted by *Wetzler et al*. [1998] in puff model results. A related fact is that the maximum flux of *C*

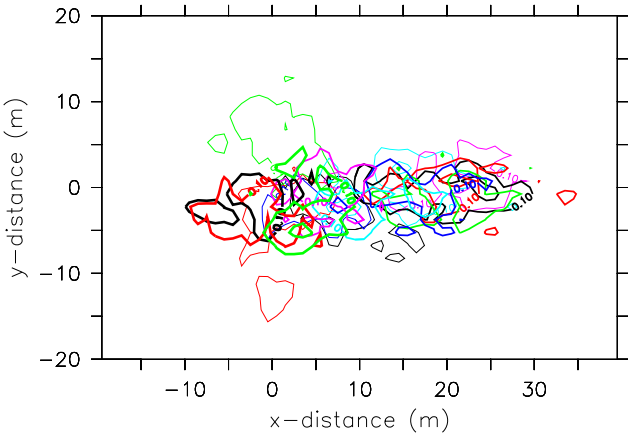

Figure 8. Contours of the vertical velocity isopleth 0.1 m s^{-1} on the *x*-*y* plane at $z = 2155$ m at different times, represented by difference colors, over a full cycle of oscillatory cross flow. Exp. 17.

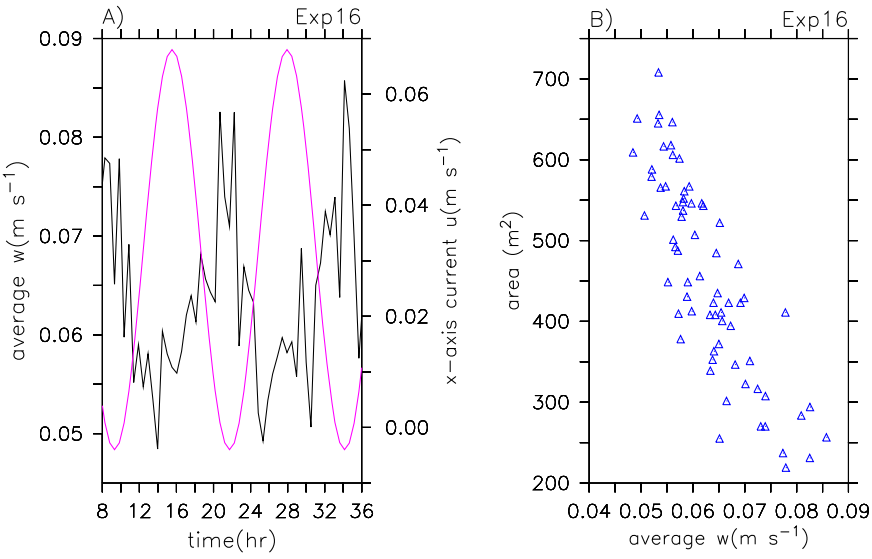

Figure 9. (a) Vertical velocity $\langle w \rangle$ in the plume at $z = 2155$ m (black) superimposed on the horizontal velocity (u) of the background flow (purple). $\langle w \rangle$ is the areal average of w over the region on the plane $z = 2155$ m where $w > 0.02$ cm s^{-1}. (b) The correspondence between $\langle w \rangle$ at 2155 m and the area of upflow, in each case for computational cells where $w > 0.02$ cm s^{-1}. Exp. 16.

through the right domain boundary does not occur at the time of largest flow velocity.

[38] Figures 10a and 10c are instances when x axis speeds are identical, but in one case, flow is accelerating, while in the other, the flow is decelerating. The obvious differences in plume concentrations and shape in these two plots will show up as hystersis when selected plume variables are plotted against cross flow speeds over a full-cycle duration [e.g., *Di Iorio et al.*, 2012]. With M_2 tidal velocities at the seafloor often as large or larger than mean or long period flows, the likelihood of similar sequences of plume patterns in the real ocean is reasonably high.

[39] The mass of C per unit depth within the computational domain at various cross-flow acceleration stages demonstrates the same result (Figure 11a). Here C integrated over x (-56 m $< x <$ 120 m) and y (-84 m $< y <$ 84 m) is plotted versus depth. Three instances each at times of slack flow decelerating and slack flow accelerating all show plume C mass within the near field (computational domain) is larger at times of minimum rather than maximum cross flow. In addition, more mass is present after slack flow when flow is accelerating than before.

[40] Areal-averaged mass and mass flux at the downstream boundary (Figure 11b) show the large amplitude variability of each, consistent with the arrival of C accumulated during slack water and its passage out of the domain. Both variables are 10 times their minimum values as accumulated C advects through that plane. The u velocity, without an absolute scale, is superimposed (Figure 11b). Comparing pairs of curves show that maximum flux and maximum tracer mass within the domain occur as the cross flow accelerates. Minimum values (small negative) occur at

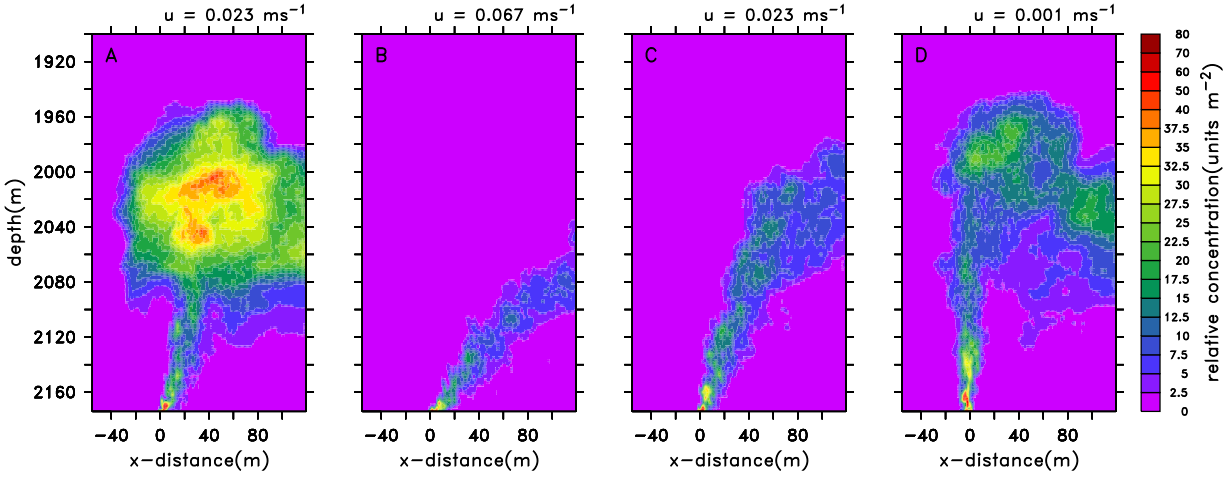

Figure 10. Dynamically inactive tracer C, integrated over the y direction, at four instances during the cyclic cross flow. Concentration units are arbitrary but identical across all plots. Exp. 17.

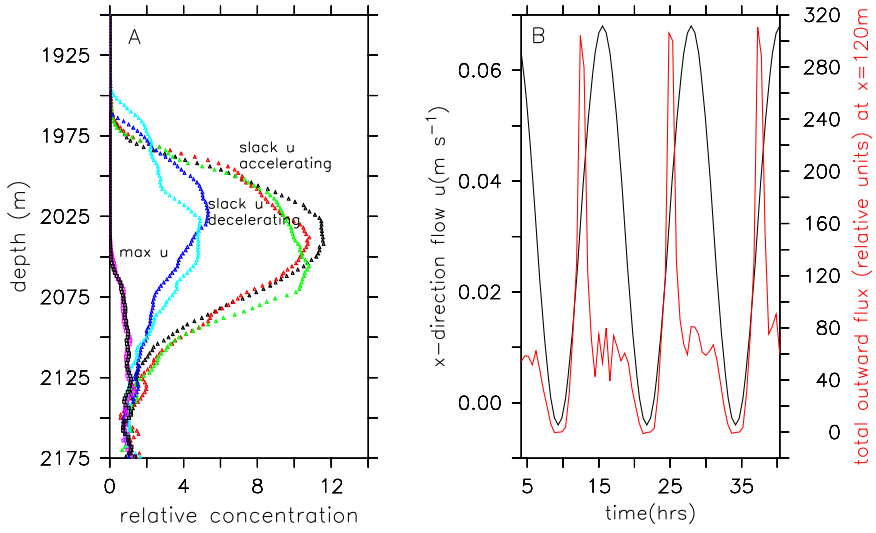

Figure 11. (a) Profiles of C integrated over the *x*-*y* plane extending laterally $-56\ \text{m} < x < 120\ \text{m}$, $y = -84\ \text{m} < y < 84\ \text{m}$ for each of three time periods: near slack water after flow deceleration, near slack water as cross flow begins to accelerate, and when cross-flow velocity is at a maximum. (b) Time series of cross flow (black) and mass flux (red) averaged over the vertical *y*-*z* plane extending $-84\ \text{m} < y < 84\ \text{m}$ and $1851\ \text{m} < z < 2175\ \text{m}$ at the downstream exit ($x = 120$ m). Exp. 16.

the time of smallest cross flow (equations (11) and (12)). The differences in fluxes and integrated C at these two times of identical cross flows reemphasize the hysteresis in the convection-transport process.

4.2. Fine-Scale Variability

[41] As the plume moves downstream it spreads laterally. Figure 12 images the dynamically inactive tracer C, the vertical velocity w, and the density gradient from Exp. 19 at a point 25 m downstream of the source. At this site and time, the plume reaches to 1900 m height and has a cap spread of nearly 160 m. The large spatial variability of the signal is apparent in all plots. The vertical velocity still exceeds 0.1 m s^{-1} upward in the core of the rising plume, but down-flow is evident on both outer edges of the plume cap (Figure 12b). Density gradient anomalies are shaded in Figure 12c. Unstable stratification (negative gradient) occurs throughout the plume region, but particularly in the lower plume of this downstream cross section. Along a ribbon at the upper edge of the plume cap, stratification is stable (Figure 12c). Individual unstably stratified fluid cells randomly occur just below that ribbon, suggesting that in the upper reaches of the cap, density overturning continues to occur there.

[42] Fine-scale variability occurs in the time domain as well. Figure 13 depicts three 1 h time series taken around a time of minimum decelerating cross flow when the plume is most vertical. Velocity w was sampled at $z = 2155$ m and at neighboring points around $x = 0$, $y = 0$ (see figure caption). The mean upward flow for all three time series is 0.12 m s^{-1} with a standard deviation of 0.064 m s^{-1}.

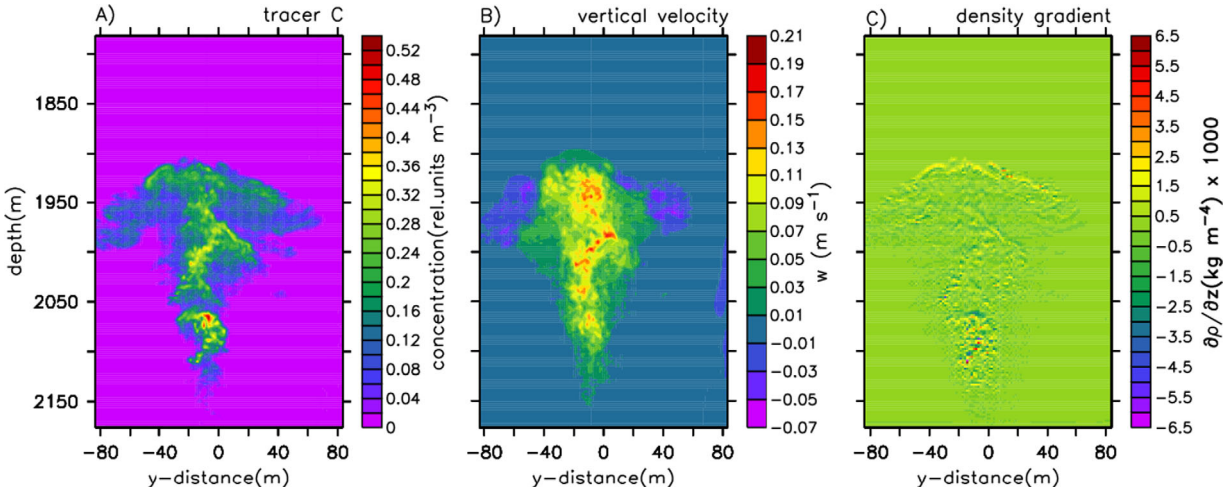

Figure 12. *y*-*z* cross sections downstream of the source at $x = 25$ m for C, w, and dρ/dz. Exp. 19.

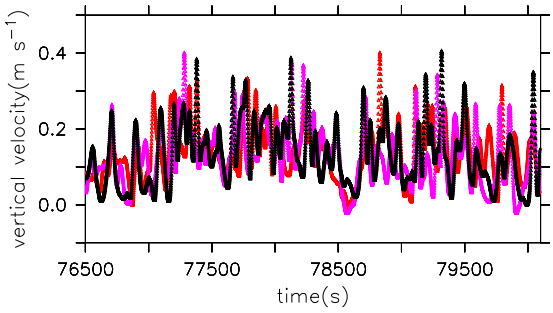

Figure 13. A *1* h time series sampled every second of model vertical velocity within the plume core at $z = 2155$ m, $y = 0$, and $x = +0.5$ m (black), $x = -0.5$ m (red) and $x = 1.5$ m (purple). Exp. 17.

4.3. Dependence on Hydrography

[43] Experiments that differ only in background hydrography also yield plumes of different vertical reach (Figures 14a and 14b). Nonlinear hydrography (Figure 1) has smaller vertical gradients than linear hydrography in the initial 225 m above bottom, but similar slopes above that. The smaller near-source gradients should allow faster rise, less dilution, and thus higher rise height. Larger vertical velocities in the stem should also result in some differences in the degree to which the plume bends in the cross flow.

[44] Juxtaposing results from Exps. 17 and 19 (Table 1) shows that, indeed, the two plumes (Figures 14a and 14b) are noticeably different in vertical reach. Linear hydrography (Figure 1) with its larger gradients in the lowest 200 m slows and stops plume rise in a shorter vertical distance. On the plane $z = 2100$, the *average* upflow for all cells where $w > 0.02$ m s^{-1} is 6.9 cm s^{-1} (linear hydro) and 7.7 cm s^{-1} (nonlinear hydro), while the *maximum* upflows on the same plane were 20.5 and 25.2 cm s^{-1}, respectively. Higher above the source on the plane $z = 1950$ m, average w in upflows >0.020 m s^{-1} is 2.5 cm s^{-1} (linear hydro) versus 6.4 cm s^{-1} (nonlinear hydro).

[45] Plumes expressed via tracer C (Figures 14c and 14d) show differences in rise heights by ~30 m. If plume rise height were to be used to infer source buoyancy flux, a difference in rise heights by ~30 m (Figures 14c and 14d) would make a difference in buoyancy flux estimates by a factor of 1.6. The hydrographic differences do change the degree to which the plume is bent over by the cross flow (not shown). Nonlinear hydrography permits larger upflows near the source, yielding a tilt angle of 47°. Linear hydrography with larger vertical gradients and smaller upflow velocities during the initial part of the ascent bends plumes from the vertical by 52°, both at times of largest cross flow.

4.4. Entrainment

[46] Unlike integral models [e.g., *Morton et al*., 1956; *Hoult and Weil*, 1972], numerical convection models do not require an entrainment parameterization, but it is nonetheless true that ambient fluid is drawn into the plumes during buoyant ascent. Convection model results can consequently be cast into an entrainment parameterization framework. Effective entrainment coefficients are derived here for plumes experiencing nearly still cross flow, the setting for the model of *Morton et al*. [1956]. Derivation of effective entrainment coefficients when the plume is bent over by a cross flow [e.g., *Hoult and Weil*, 1972] is left for a later time.

[47] Vertical velocities exceeding 0.02 m s^{-1} on the horizontal plane at 2155 m (20 mab) during a time of negligible cross flow (Figure 15) show an irregularly shaped plume footprint. The circle in light blue (Figure 15), centered at the w velocity weighted "center of mass" (x_C, y_C) has an area identical to that of the footprint. The radius of that circle will be designated r_{EFF}. Around that same circle, horizontal flow vectors have also been drawn (Figure 15), the largest of which represents a speed of 0.054 m s^{-1}.

[48] In the integral model of *Morton et al*. [1956], horizontal flow is radial into a plume stem having a circular cross section. In our turbulent convection model experiments, the cross section is never circular. Moreover, while

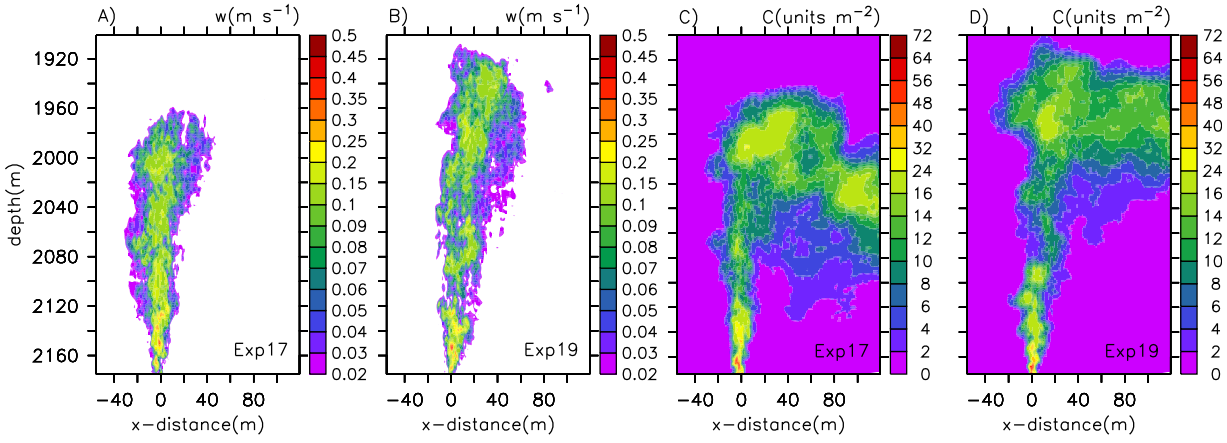

Figure 14. (a and b) Vertical velocity on the plane $y = 0$ during a time of minimum cross flow from Exps. 17 and 19. (c and d) Concentrations of tracer C integrated from -84 m $< y <$ 84 m for Exps. 17 and 19. Differences in Figures 14a to 14b and Figures 14c to 14d are caused entirely by the differences in the hydrographic profiles depicted in Figure 1. The height of the model domain in both cases (Table 1) exceeds the height interval shown.

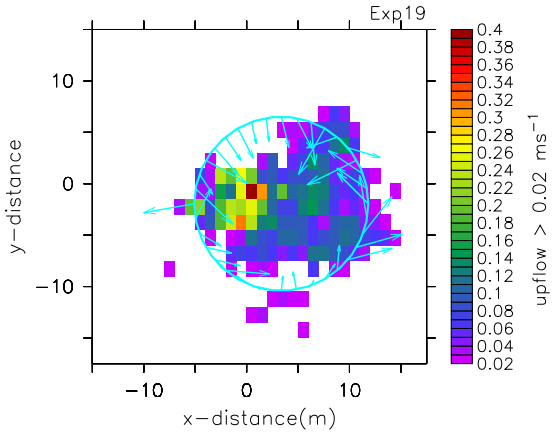

Figure 15. Vertical velocity >0.02 m s^{-1} on a plane 20 m above the venting source. The area where $w > 0.02$ m s^{-1} is represented by a circle of equivalent area centered at the w "center of mass" ($x = 3.4$ m, $y = -1.9$ m). Vectors indicate horizontal velocity across that circular boundary. The largest vector represents flow at 5.4 cm s^{-1}. Exp. 19.

the overall sense of horizontal fluid flux is inward, not all vectors are radially directed or inward. A few are outward or nearly tangential to the circle. Entrained flow as depicted in Figure 15 also changes rapidly in time.

[49] The effective radius (and upward flux, w_{FLUX}, and flux perimeter, S_{EFF}) for the plume was calculated at each of 38 equally separated levels between 2099 and 2173 m and over three separate time intervals ($\Delta t = 12.42$ h) centered at $t = 8.333$, 20.75, and 33.17 h. At those times, cross-flow speed was negligible and decelerating and the plume was nearly upright. Around each of those times, six hundred 1 s sample values of r_{EFF} (and w_{FLUX} and S_{EFF}) were calculated. Samples were then time-averaged over each 600 s interval, providing three data points at each of 38 depths ($N = 114$).

[50] Figure 16a shows the resulting r_{EFF} ranging from ~4 m to >17 m over 2–76 m of plume rise. r_{EFF} has a strong correlation with depth. A least square fit of the form:

$$r_{EFF} = \beta(z_0 - z) \tag{16}$$

to the data yields the values $\beta = 0.162 \mp 0.006$, and $z_0 = 2203$ m $\mp$ 2.6 m. The slope β is called the expansion rate [e.g., *Rona et al*., 2002]. The variable z_0 is the depth of a virtual source point, virtual because it represents the depth at which the source has zero radius. The unrealistically large value of z_0 may be the consequence of the apparent nonlinearity of r_{EFF} in the 5 m nearest the seafloor (Figure 16a). The value of β is in line with previous estimates of β for other plumes at other hydrothermal sites. At the venting edifice called Monolith, *Bemis et al*. [2002] found a β value varying between 0.088 and 0.130. *Rona et al*.'s [2002] value for β from EPR 21°N measurements was 0.2 and *Xu and Di Iorio*'s [2012] integral model expansion rate estimate for Dante was 0.196.

[51] In like fashion, 114 upward flux (w_{FLUX}) values were calculated, three each at 38 depths. Plume edge cutoff

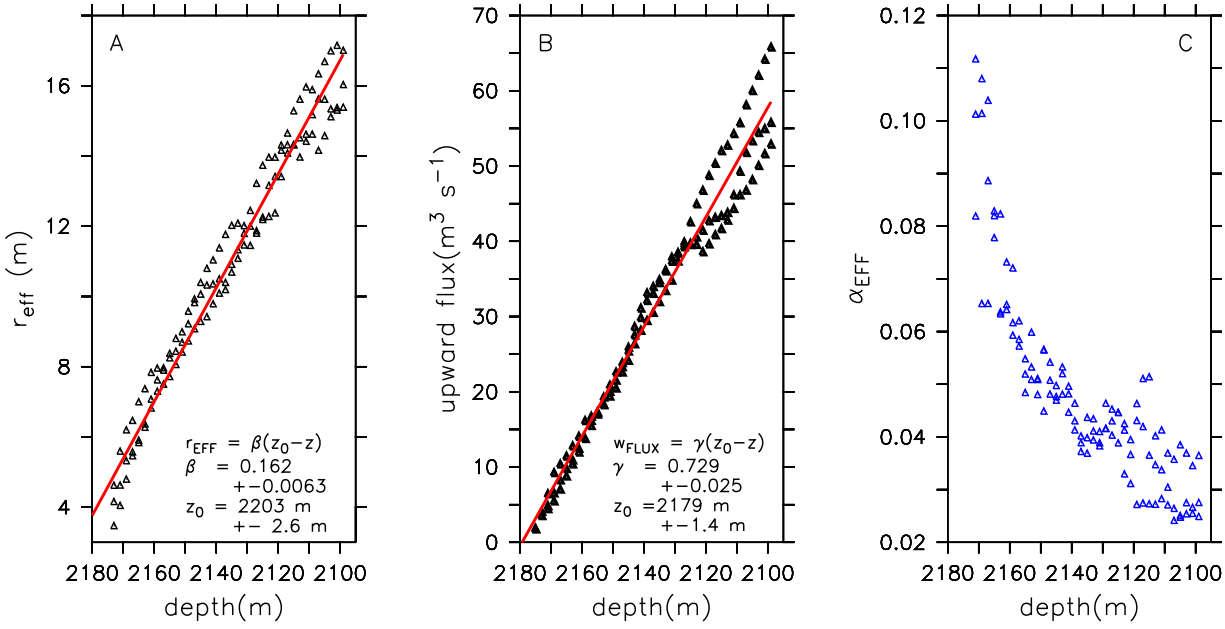

Figure 16. (a) Effective radius (r_{EFF}) and (b) the upward flux as functions of depth in the lower reaches of the plume in Exp. 19. Plume edge criterion was $w > 0.02$ cm s^{-1}. Six hundred 1 s sampled values at each of three separate ($\Delta t = 12.42$ h) times ($t = 8.333$, 20.75, and 33.17 h) were time-averaged to provide three data points at each of 38 depths between 2099 and 2173 m ($N = 114$). Central sampling times were chosen so as to capture data when cross-flow speed was negligible and the plume was nearly upright. Slopes, intercepts, and 95% confidence intervals are indicated. (c) The effective entrainment coefficient, α_{EFF}, as a function of depth derived using equation (18).

criterion remained $w = 0.02$ m s^{-1}. The flux results plotted against height (Figure 16b) also showed the relationship to be linear. When least squares fit with a form analogous to equation (16), the line slope was found to be 0.729 $\mp$ 0.025, while the virtual source depth z_0 was a more reasonable 2179 m $\mp$ 1.4 m. With w_{FLUX} proportional to z, the vertical gradient of w_{FLUX} is just the best fit slope (0.729).

[52] The plume radius increasing with height is a result of fluid being drawn, or entrained, into the plume at each level. Using an inverted truncated cone as a control volume, *Morton et al*. [1956] used Gauss's theorem to require that the difference in mass flux (for constant density) through the upper and lower control volume surfaces be equal the flux entering the control volume circumferentially:

$$\frac{d}{dz}\pi r^2\langle w\rangle = 2\pi r\langle u_r\rangle = (2\pi r)\alpha_{EFF}\langle w\rangle \tag{17}$$

where r is the radius of the volume element at height z, $\langle w\rangle$ is the cross-sectionally averaged w into and out of the volume element, and $\langle u_r\rangle$ is a circumferentially averaged radial inflow velocity. The seminal step in the *Morton et al*. [1956] paper was the closure assumption, i.e., the replacement of u_r in equation (17) by the product of an entrainment coefficient, α_{EFF} and $\langle w\rangle$.

[53] In the irregular pattern of the upflow areas as exemplified in Figure 15, the generalization of equation (17) is

$$\frac{d}{\mathrm{d}z}\int w\,\mathrm{d}A = \int \vec{v}\cdot\vec{n}\,\mathrm{d}s = \alpha_{EFF}\langle w\rangle\int\frac{\vec{v}\cdot\vec{n}}{|\vec{v}\cdot\vec{n}|}\,\mathrm{d}s = \alpha_{EFF}\langle w\rangle S_{EFF} \tag{18}$$

where dA (= dx dy) is the horizontal area of a computational cell, w is the upflow across that surface, $\vec{v}$ is a horizontal flow vector, $\vec{n}$ is a unit vector normal to each cell side, ds is a cell edge distance (dx or dy), and S_{EFF} is the total perimeter length of w_{FLUX}. Integrals are only over cells meeting the threshold condition. The effective entrainment coefficient, α_{EFF}, represents the extension of the *Morton et al*. [1956] closure idea to the case of irregularly shaped upflow areas (Figure 15). Equation (18) allows α_{EFF} to be determined when the vertical gradient of the upward flux, the average vertical velocity $\langle w\rangle$ over the plume cross section, and the length of the plume perimeter S_{EFF} are known.

[54] S_{EFF} was determined for each of 38 depth levels (2173 m–2099 m) and three time intervals in a manner analogous to the w_{FLUX} and r_{EFF} calculations. Dividing the flux gradient by the product of $\langle w\rangle$ and S_{EFF} (equation (18)) for each of 114 cases results in α_{EFF} values that decrease from 0.11 to ~0.025 with increasing height (2–76 m) above the source (Figure 16c). At a height of 76 m above the source, the average of three samples for α_{EFF} is 0.030 (Figure 16c).

[55] The range of our α_{EFF} values includes the value (0.0833) often chosen as the entrainment constant for buoyant convection in still, stratified environments [*List*, 1982]. Smaller values are often used in the case of buoyant jets entering otherwise still environments. The variation of α_{EFF} with height was previously observed in results of an axisymmetric convection model of a starting plume [*Lavelle and Baker*, 1994]. In that study, α_{EFF} fell from maximum values at source depth to negative values in the plume cap where the *Morton et al*. [1956] entrainment assumption clearly no longer holds. *Carazzo et al*. [2008] examined the effects of variable entrainment rates on rise heights in stratified but otherwise calm environments and found that source fluxes might be underestimated by factors of two or more if variable entrainment was not taken into account.

5. Summary and Conclusions

[56] Plumes bent by time-variable cross flows result in rise heights that are never constant and concentration at fixed points downstream that are never quasi steady. Time-variable cross flows cause pooling of effluent above the source point, which leads to higher rise heights at times of weak flow, and results in streaming of effluent away from the source and smaller rise heights at times of strong flow. The consequence is property anomalies in the form of boluses of fluid that are intermittently, if not periodically, advected downstream and away from a source region. The near-ubiquitous nature of M_2 tidal currents in the ocean make this hydrothermal plume configuration one of the most likely to be observed.

[57] The turbulent nature of the model yields plumes with cross sectional and height variance qualitatively like those observed acoustically in the field. Model results show flow into the plume stem at any level is not azimuthally invariant, or even always directed inward at every point on the plume stem wall. Entrainment, as represented by an effective entrainment coefficient, shows variability with height above the source.

[58] Differences in rise height at minimum flow between cases that differ only slightly in background stratification (e.g., Figure 1) are considerable. Accurately estimating hydrothermal buoyancy flux (B_0) is thus even more problematic than caused by the weak theoretical dependence of rise heights on B_0 for linearly stratified environments. Vertical velocity in the lower part of the buoyant plume is a more sensitive indicator of source flux.

[59] Model studies, as in this paper, of the conditions favoring plume bifurcation [e.g., *Lavelle*, 1997] or plume puffing at a fixed frequency [*Cetegen and Ahmed*, 1993] are possible next steps. Does the unsteadiness of the cross flow prevent both or either from happening? Additional studies of the effects of an Ekman boundary layer and rotation are worthy substudies as well. The new cabled observatories (e.g., *Barnes et al*. [2011]; http://www.oceanobservatories.org/infrastructure/ooi-station-map/regional-scale-nodes/) will greatly change the density of data coming from hydrothermal source regions, providing, e.g., long high-frequency time series measurements of velocities, turbulence, heat, and chemical concentrations. Numerical turbulent convection models of this kind will undoubtedly prove useful in unraveling complexities in those new data sets.

[60] **Acknowledgments.** We thank G. Xu of Rutgers University for creating Figure 3 using COVIS data and R. Light and M. Kenney of the Applied Physics Laboratory at the University of Washington for the engineering design and implementation of COVIS that make that image possible. Two anonymous reviewers are thanked for their constructive comments. J. W. Lavelle's work has been supported by the NOAA/Pacific

Marine Environmental Laboratory and by NOAA's VENTS program. D. D. has been supported by NSF under the CAREER grant OCE0449578. P. R. acknowledges support from NSF grants OTIC 0825088 and OCE 1234141. The freeware tool Ferret was used for the analyses and graphing of data. PMEL contribution 4000.

References

Asselin, R. A. (1972), Frequency filters for time integrations, *Mon. Weather Rev.*, *100*(6), 487–490.

Barnes, C. R., M. Best, F. R. Johnson, L. Pautet, and B. Pirenne (2011), Understanding Earth/ocean processes using real-time data from NEPTUNE Canada's widely distributed sensor networks, north-east Pacific, *Geosci. Can.*, *38*(1), 21–30.

Bemis, K., D. Silver, P. Rona, and J. Cowen (2006), A particle sedimentation model of buoyant jets: Observations of hydrothermal plumes, *Cah. Biol. Mar.*, *47*, 379–384.

Bemis, K. G., R. P. Von Herzen, and M. J. Mottl (1993), Geothermal heat-flux from hydrothermal plumes on the Juan-de-Fuca Ridge, *J. Geophys. Res.*, *98*, 6351–6365, doi:10.1029/92JB02273.

Bemis, K. G., P. A. Rona, D. Jackson, C. Jones, D. Silver, and K. Mitsuzawa (2002), A comparison of black smoker hydrothermal plume behavior at Monolith Vent and at Clam Acres Vent Field: Dependence on source configuration, *Mar. Geophys. Res.*, *23*(2), 81–96, doi:10.1023/A:1022484931681.

Berdeal, I. G., S. L. Hautula, L. N. Thomas, and H. P. Johnson (2006), Vertical structure of time-dependent currents in a mid-ocean ridge axial valley, *Deep Sea Res., Part I*, *53*, 367–386, doi:10.1016/j.dsr/2005.10.004.

Bischoff, J. L., and R. J. Rosenbauer (1985), An empirical equation of state for hydrothermal seawater (3.2% NaCl), *Am. J. Sci.*, *285*, 725–763.

Burnham, C. W., J. R. Holloway, and N. F. Davis (1969), Thermodynamic properties of water to 1000°C abd 10,000 bars, *Spec. Pap. Geol. Soc. Am.*, *132*, 96 pp, Geological Society of America, Boulder , Col.

Butterfield, D. A., R. E. McDuff, M. J. Mottl, M. D. Lilley, J. E. Lupton, and G. J. Massoth (1994), Gradients in the composition of hydrothermal fluids from the Endeavour segment vent field: Phase separation and brine loss, *J. Geophys. Res.*, *99*, 9561-9583.

Carazzo, G., E. Kaminski, and S. Tait (2008), On the rise of turbulent plumes: Quantitative effects of variable entrainment of submarine hydrothermal plumes, terrestrial and extra terrestrial explosive volcanism, *J. Geophys. Res.*, *113*, B09201, doi:10.1029/2007JB005458.

Cetegen, B. M., and T. A. Ahmed (1993), Experiments on the periodic instability of buoyant plumes and pool fires, *Combust. Flame*, *93*(1–2), 157–184, doi:10.1016/0010–2180(93)90090-P.

Cruse, A. M., and J. S. Seewald (2010), Low-molecular weight hydrocarbons in vent fluids from the Main Endeavour Field, northern Juan de Fuca Ridge, *Geochim. Cosmochim. Acta*, *74*(21), 6126–6140, doi:10.1016/j.gca.2010.07.013.

Delaney, J. R., V. Robigou, R. E. McDuff, and M. K. Tivey (1992), Geology of a vigorous hydrothermal system on the Endeavour Segment, Juan de Fuca Ridge, *J. Geophys. Res.*, *97*, 19,663–19,682.

Delaney, J. R., D. S. Kelley, M. D. Lilley, D. A. Butterfield, R. E. Duff, J. A. Baross, J. W. Deming, H. P. Johnson, and V. Robigou (1997), The Endeavour hydrothermal system I: Cellular circulation above an active cracking front yields large sulfide structures, 'fresh' vent water, and hyperthermophilic archaea, *Ridge Events*, *8*, 11–19.

Devenish, B. J., G. Rooney, H. Webster, and D. Thomson (2010), The entrainment rate for buoyant plumes in a crossflow, *Boundary Layer Meteorol.*, *134*, 411–439.

Di Iorio, D., J. W. Lavelle, P. A. Rona, K. Bemis, G. Y. Xu, L. N. Germanovich, R. P. Lowell, and G. Genc (2012), Measurements and models of heat flux and plumes from hydrothermal discharges near the deep seafloor, *Oceanography*, *25*(1), 168–179, doi:10.5670/oceanog.2012.14.

Fay, J. A. (1973), Buoyant plumes and wakes, *Annu. Rev. Fluid Mech.*, *5*, 151–160, doi:10.1146/annurev.fl.05.010173.001055.

Fofonoff, N. P., and R. C. Millard, Jr. (1983), Algorithms for computation of fundamental properties of seawater, *UNESCO Tech. Pap. Mar Sci., 44*, 53 pp., UNESCO, Paris.

German, C. R., D. R. Yoerger, M. Jakuba, T. M. Shank, C. H. Langmuir, and K. Nakamura (2008), Hydrothermal exploration with the Autonomous Benthic Explorer, *Deep Sea Res., Part I*, *55*, 203–219, doi:10.1016/j.dsr.2007.11.004.

Ginster, U., and M. J. Mottl (1994), Heat flux from black smokers on the Endeavour and Cleft segments, Juan de Fuca Ridge, *J. Geophys. Res.*, *99*, 4937–4950.

Glickson, D. A., D. S. Kelley, and J. R. Delaney (2007), Geology and hydrothermal evolution of the Mothra Hydrothermal Field, Endeavor Segment, Juan de Fuca Ridge, *Geochem. Geophys. Geosyst.*, *8*, Q06010, doi:10.1029/2007GC001588.

Hanna, S. R., G. A. Briggs, and R. P. Hosker Jr. (1982), *Handbook of Atmospheric Diffusion*, 102 pp., Tech Inf. Cent., U.S. Dep. of Energy, Washington, D. C.

Harlow, F. H., and J. E. Welch (1965), Numerical calculation of time-dependent viscous incompressible flow of fluid with a free surface, *Phys. Fluids*, *8*(12), 2182–2189.

Hoult, D. P., and J. C. Weil (1972), Turbulent plume in a laminar cross flow, *Atmos. Environ.*, *6*(8), 513–530, doi:10.1016/0004-6981(72)90069-8.

Jackson, D. R., C. D. Jones, P. A. Rona, and K. G. Bemis (2003), A method for Doppler Acoustic measurement of black smoker flow fields, *Geochem. Geophys. Geosyst.*, *4*(11), 1095, doi:10.1029/2003GC000509.

Johnson, H. P., M. A. Tivey, T. A. Bjorkland, and M. S. Salmi (2010), Hydrothermal circulation within the Endeavour Segment, Juan de Fuca Ridge, *Geochem. Geophys. Geosyst.*, *11*, Q05002, doi:10.1029/2009GC002957.

Kaye, N. B., and P. F. Linden (2004), Coalescing axisymmetric turbulent plumes, *J. Fluid Mech.*, *502*, 41–63.

Kelley, D. S., et al. (2012), Endeavour Segment of the Juan de Fuca Ridge: One of the most remarkable places on earth, *Oceanography*, *25*(1), 44–61.

Kremer, D. M., M. T. am Ende, J. G. Mustakis, and D. J. am Ende (2007), A numerical investigation of a jet in an oscillating crossflow, *Phys. Fluids*, *19*, 095103, doi:10.1063/1.2770523.

Kunze, E., and T. B. Sanford (1996), Abyssal mixing: Where it is not, *J. Phys. Oceanogr.*, *26*, 2286–2296.

Lavelle, J. W. (1997), Buoyancy driven plumes in rotating, stratified cross flows: Plume dependence on rotation, turbulent mixing, and cross-flow strength, *J. Geophys. Res.*, *102*, 3405–3420.

Lavelle, J. W., and E. T. Baker (1994), A numerical study of local convection in the benthic ocean induced by episodic hydrothermal discharges, *J. Geophys. Res.*, *99*, 16,065–16,080.

Lavelle, J. W., and W. C. Thacker (2008), A pretty good sponge: Dealing with open boundaries in limited-area ocean models, *Ocean Modell.*, *20*(3), 270–292, doi:10.1016/j.ocemod.2007.10.002.

Lavelle, J. W., and M. A. Wetzler (1999), Diffuse venting and background contributions to chemical anomalies in a neutrally buoyant ocean hydrothermal plume, *J. Geophys. Res.*, *104*, 3201–3209, doi:10.1029/1998JC900063.

Ledwell, J. R., A. J. Watson, and C. S. Law (1993), Evidence for slow mixing across the pycnocline from an open-ocean tracer-release experiment, *Nature*, *364*, 701–703.

List, E. J. (1982), Turbulent jets and plumes, *Annu. Rev. Fluid. Mech.*, *14*, 189–212.

Mahesh, K. (2013), The interaction of jets with crossflow, *Annu. Rev. Fluid Mech.*, *45*, 379–407, doi:10.1146/annurev-fluid-120710-101115.

Merle, S. (Ed.) (2006), NeMO 2006 Cruise Report, NOAA Vents Program, Axial Volcano and the Endeavour Segment, Juan de Fuca Ridge, R/V THOMPSON Cruise TN-199, 22 August–7 September 2006. Seattle WA to Seattle WA; ROPOS dives R1008–R1014, NOAA/Pacific Marine Environmental Laboratory, Seattle, Wash. [Available at http://www.pmel.noaa.gov/vents/nemo2006/nemo06-crrpt-final.pdf.]

Morton, B., G. I. Taylor, and J. Turner (1956), Turbulent gravitational convection from maintained and instantaneous sources, *Proc. R. Soc. London, Ser. A*, *234*, 1–23.

Rona, P., and R. Light (2011), Sonar images hydrothermal vents in seafloor observatory, *Eos Trans. AGU*, *92*(20), 169, doi:10.1029/2011EO200002.

Rona, P. A., D. R. Palmer, C. Jones, D. A. Chayes, M. Czarnecki, E. W. Carey, and J. C. Guerrero (1991), Acoustic imaging of hydrothermal plumes, East Pacific Rise, 21°N, 109°W, *Geophys. Res. Lett.*, *18*, 2233–2236, doi:10.1029/91GL02897.

Rona, P. A., K. G. Bemis, D. Silver, and C. D. Jones (2002), Acoustic imaging, visualization, and quantification of buoyant hydrothermal plumes in the ocean, *Mar. Geophys. Res.*, *23*(2), 147–168, doi:10.1023/A:1022481315125.

Rona, P. A., K. G. Bemis, C. D. Jones, D. R. Jackson, K. Mitsuzawa, and D. Silver (2006), Entrainment and bending in a major hydrothermal plume, Main Endeavour Field, Juan de Fuca Ridge, *Geophys. Res. Lett.*, *33*, L19313, doi:10.1029/2006GL027211.

Rudnicki, M. D., R. H. James, and H. Elderfield (1994), Near-field variability of the TAG non-buoyant plume, 26°N, Mid-Atlantic Ridge, *Earth Planet. Sci. Lett.*, *127*(1–4), 1–10.

Smagorinsky, J. (1993), Some historical remarks on the use of nonlinear viscosities, in *Large Eddy Simulation of Complex Engineering and Geophysical Flows*, edited by B. Galperin and S. A. Orszag, pp. 3–36, Cambridge Univ. Press, New York.

Smolarkiewicz, P. K., and L. G. Margolin (1998), MPDATA: A finite-difference solver for geophysical flows, *J. Comput. Phys.*, *140*, 459–480.

Stahr, F. R., R. E. McDuff, D. R. Yoerger, A. M. Bradley, and K. Nakamura (2000), Heat flux measurements at the Main Endeavour vent field, Juan de Fuca Ridge, *Eos Trans. AGU*, *81*(48), Fall Meet. Suppl., Abstract OS52I-03.

Tao, Y., S. Rosswog, and M. Brüggen (2013), A simulation modeling approach to hydrothermal plumes and its comparison to analytical models, *Ocean Modell.*, *61*, 68–80, doi:10.1016/j.ocemod.2012.10.001.

Thomson, R. E., S. F. Mihaly, A. B. Rabinovich, R. E. Mcduff, S. R. Veirs, and F. R. Stahr (2003), Constrained circulation at Endeavour Ridge facilitates colonization by vent larvae, *Nature*, *424*(6948), 545–549.

Thomson, R. E., M. M. Subbotina, and M. V. Anisimov (2005), Numerical simulation of hydrothermal vent-induced circulation at Endeavour Ridge, *J. Geophys. Res.*, *110*, C11011, doi:10.1029/2004JC002337.

Venayagamoorthy, S. K., and D. D. Stretch (2010), On the turbulent Prandtl number in homogenous stably stratified turbulence, *J. Fluid Mech.*, *644*, 359–369.

Veirs, S. R. (2003), Heat flux and hydrography at a submarine volcano: Observations and models of the Main Endeavour vent field in the Northeast Pacific, PhD thesis, 209 pp., Univ. of Washington, Seattle.

Veirs, S. R., R. E. McDuff, and F. T. Stahr (2006), Magnitude and variance of new bottom horizontal heat flux at the Main Endeavour hydrothermal vent field, *Geochem. Geophys. Geosyst.*, *7*, Q02004, doi:10.1029/2005GC000952.

Wetzler, M. A., J. W. Lavelle, G. A. Cannon, and E. T. Baker (1998), Variability of temperature and currents measured near Pipe Organ hydrothermal vent site, *Mar. Geophys. Res.*, *20*(6), 505–516, doi:10.1023/A:1004784405430.

Woods, A. W. (2010), Turbulent plumes in nature, *Annu. Rev. Fluid Mech.*, *42*, 391–412, doi:10.1146/annurev-fluid-121108-14543.

Xia, L., and K. Lam (2004), Unsteady effluent dispersion in a round jet interacting with an oscillating cross-flow, *J. Hydraul. Eng.*, *130*(7), 667–677, doi:10.1061/(ASCE)0733-9429(2004)130:7(667).

Xu, G. Y., and D. Di Iorio (2011), The relative effects of particles and turbulence on acoustic scattering from deep-sea hydrothermal vent plumes, *J. Acoust. Soc. Am.*, *130*(4), 1856–1867, doi:10.1121/1.3624816.

Xu, G. Y., and D. Di Iorio (2012), Deep sea hydrothermal plumes and their interaction with oscillatory flows, *Geochem. Geophys. Geosyst.*, *13*, Q0AJ01, doi:10.1029/2012GC004188.

Xu, G., D. R. Jackson, K. G. Bemis, and P. A. Rona (2013), Observations of the volume flux of a seafloor hydrothermal plume using an acoustic imaging device, *Geochem. Geophys., Geosyst.*, *14*, 2369–2382, doi:10.1002/ggge.20177.

Yamamoto, H., C. Cenedese, and C. P. Caulfield (2011), Laboratory experiments on two coalescing axisymmetric turbulent plumes in a rotating fluid, *Phys. Fluids*, *23*, 056601, doi:10.1063/1.3584134.